Polymer Testing 148 (2025) 108843

Contents lists available at ScienceDirect

Polymer Testing

journal homepage: www.elsevier.com/locate/polytest

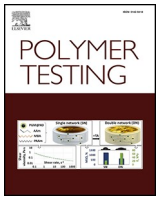

# Measurement and simulation of broadband radar absorption properties of polypyrrole nanotubes and their carbonaceous analogues

Tomáš Zálabský [a], Drahomír Čadek [b], Fatima Hassouna [a,c], Jiří Tuček [a], Tomáš Lapka [c], Dušan Kopecký [a,c,*]

[a] Faculty of Electrical Engineering and Informatics, University of Pardubice, 532 10, Pardubice, Czech Republic
[b] Faculty of Chemical Technology, University of Chemistry and Technology, Prague 6, 166 28, Prague, Czech Republic
[c] Faculty of Chemical Engineering, University of Chemistry and Technology, Prague 6, 166 28, Prague, Czech Republic

ARTICLE INFO

*Keywords:*
Radar absorbing materials
Electromagnetic interference shielding
Polypyrrole nanotubes
Carbon nanotubes
Waveguide method
Scattering parameters
Permittivity

ABSTRACT

The rapid development of unmanned aerial and ground vehicles (UAVs and UGVs, respectively) requires innovative means for their protection against detection and localization by radar microwave signals. Radar absorbing materials (RAMs) used in functional or structural composites of small, low-speed UAVs and UGVs can employ non-conventional fillers, such as nanostructured conductive polymers or their carbonaceous analogues. However, the work with non-conventional fillers brings difficulties in preparation and manipulation with sufficient amounts on a laboratory scale in a reasonable time and at a reasonable price. Therefore, computer simulation of filler behavior using software tools can be a vital solution to assess their ability to serve as RAMs. Here, polypyrrole nanotubes (PPy-NT) and carbonized polypyrrole nanotubes (PPy-C) were dispersed in polydimethylsiloxane matrix (PDMS) at low concentrations (1–3 % w/w) and their attenuation properties (reflection, absorption, and transmission coefficients), dielectric properties (complex permittivity and loss tangents) and apparent alternating current (AC) conductivity were evaluated between 2.6 GHz and 18 GHz. A 2 mm thin sample of the PPy-NT/PDMS composite at low concentration of 3 % w/w of the filler absorbs 28 % of the radar signal at 3.3 GHz. Using the simulation model made in CST Studio software, the evaluation of radar absorption properties was extended beyond the physical boundaries of the PPy-NT/PDMS sample, and the attenuation properties were evaluated up to a theoretical thickness of 100 mm (absorption of the signal 63 %). The presented method of simulation and the proposed model allows fast and flexible determination of attenuation properties of non-conventional RAMs of various thicknesses.

## 1. Introduction

The protection of devices against electromagnetic waves, i.e. electromagnetic shielding, is a highly specialized and advanced field of technological development. In practice, it is connected, namely, with electronic engineering, aerospace, navigation, medicine, construction, or military. In those areas, a reflection or absorption of electrical or magnetic components of an electromagnetic wave by the so-called electromagnetic shield is crucial for the proper operation of electronic devices and in some cases even for their sole existence [1,2].

The best-known disciplines of electromagnetic shielding are attenuation of radar signals [3] and shielding of electromagnetic interference [4]. Both disciplines have special directions, which are known by the general public and also reflected in popular culture, as, for example, stealth technologies of invisible planes [5] or electronic eavesdropping from emanated electromagnetic radiation [6]. Although these disciplines are demanding in terms of knowledge of the theoretical background, the practical implementation of electromagnetic shields is often simple. Electronic devices or buildings are usually protected by Faraday cages in the form of a heavy metal chassis or lining. Military systems also rely on functional paintings made of carbon-based absorbers [3]. The requirements on electromagnetic shielding are dictated by simple and straightforward criteria; everything has to be as simple as possible, durable, capable of mass production, and inexpensive in the best case.

However, continuous progress in the development of new electronic components, rapid evolution of the level of scientific, medical, or

* Corresponding author. Faculty of Electrical Engineering and Informatics, University of Pardubice, 532 10 Pardubice, Czech Republic.
*E-mail addresses:* tomas.zalabsky@upce.cz (T. Zálabský), cadekd@vscht.cz (D. Čadek), fatima.hassouna@upce.cz (F. Hassouna), jiri.tucek@upce.cz (J. Tuček), lapkat@vscht.cz (T. Lapka), dusan.kopecky@upce.cz (D. Kopecký).

https://doi.org/10.1016/j.polymertesting.2025.108843
Received 12 February 2025; Received in revised form 30 April 2025; Accepted 6 May 2025
Available online 7 May 2025

military equipment, and a shift toward high electronic integration and miniaturization, implementation of advanced automation including various kinds of artificial intelligence and demand for higher energy efficiency at the same time, impose new requirements on electromagnetic shields [7,8].

This trend is especially evident in the case of unmanned aerial and ground vehicles (UAVs, UGVs) for military applications. Various drones are becoming major war machines on battlefields and, to keep their dominance, they must be equipped with advanced electromagnetic shields. These shields must provide a sufficient level of radar invisibility, i.e. reduced radar (so-called radar cross section, RCS) and also thermal signature [9], to avoid detection and localization, and to be protective against electromagnetic countermeasures (especially electromagnetic pulses, EMP) at the same time [1]. Additionally, drones carry fairly limited amounts of energy and therefore any additional protection must be small or lightweight at least.

Compared to supersonic stealth aircraft, small drones travel with limited velocity and counterbalance their low speed with high maneuverability. Overall, the friction forces imposed by the atmosphere on the drone are low, which reduces the thermal and mechanical stress of the airframe, and means that electromagnetic shields can be made of a wider spectrum of materials.

Carbon-based commercial radar absorbing paintings (epoxy, silicone, or polyurethane matrices filled with carbonaceous and/or magnetic particles) are actually functional composites which are layered on the surface of protected, usually metal-based, objects [3]. Modern radar absorbing materials (RAMs) can serve in a similar way, but can also be integrated directly into polymeric frames of drones as structural composites [5].

Electrically conductive fillers of composites for electromagnetic shielding (both RAM or EMI), come from the field of metals (nonmagnetic [10] and magnetic [11,12] nanoparticles), carbon-based materials (graphene, nanotubes and carbon black [5] or carbon waste [13]), metal-carbon materials (layered MXenes [14,15], carbonyl metals [16]) and conducting polymers (especially nanotubes of polypyrrole or polyaniline or their metal composites [17,18]). The selection for a particular application is usually determined by their required concentration, way of dispersion or chemical treatment, and also by type, size, shape, aspect ratio of particles, properties of the targeted matrix, and also by thermal, magnetic, or environmental behavior [4].

The performance of conducting polymers in electromagnetic shielding is rather lower compared to those of metals, carbonaceous materials or layered absorbers and metamaterials [19,20]. The reason lies, namely, in their relatively lower electrical conductivity (usually $<100$ S cm$^{-1}$) [21]. However, their ability to be compatible with modern structural materials, i.e. with conventional polymers or biopolymers (e.g. cellulose [22]), is high, and, moreover, they are also lightweight and flexible, which is all advantageous for drone frame construction. Finally, preparation routes for nanostructures of conductive polymers using standard chemical syntheses are highly advantageous for cheap mass production [23].

Herein, the attenuation properties of polypyrrole nanotubes (PPy-NT) and their carbonaceous analogues (PPy-C) were evaluated in order to assess their ability to serve as RAMs. The measurement was carried out in the broad band of frequencies between 2.6 and 18 GHz, which covers the working range of the majority of aerial and ground radars. The targeted property was mainly their ability to attenuate electromagnetic radiation by absorption, but permittivity, loss tangents, and apparent alternating current (AC) conductivity were also calculated. Finally, computational models of PPy-NT and PPy-C samples were made in the CST Studio software based on measured properties to evaluate attenuation properties of both fillers beyond the limits of the physical sample.

## 2. Experimental

### 2.1. Chemicals

Polypyrrole nanotubes were synthesized from monomer pyrrole (purity 98 %), iron chloride hexahydrate (purity 99 %) and the structure-guiding agent methyl orange (purity 85 %). All reagents were purchased from Merck KGaA USA and used as received. Synthesis was carried out using a well-mastered chemical route described by Kopecký et al. [21]. Briefly, 2 ml of pyrrole were dissolved in 600 ml of 2.5 mM methyl orange solution. The solution was cooled to 5 °C and vigorously stirred. Then 8.3 g of iron chloride hexahydrate was dissolved in 69 ml of additional distilled water and added dropwise to the reaction solution. After 24 h, the solution was filtered and the product was cleaned with acetone using Soxhlet extraction. The final product was dried at 40 °C under vacuum. The described procedure was repeated (each resulted in approx. 1.5 g of black PPy-NT powder) until a sufficient amount of initial PPy-NT was obtained (usually tens of grams).

Carbonaceous analogues, i.e. N-doped carbon nanotubes (PPy-C), were prepared by high-temperature carbonization of PPy-NT in a nitrogen atmosphere. Usually, the ceramic combustion boat was loaded with approximately 0.5 g of PPy-NT and inserted into a tube furnace (Carbolite Gero). First, the tube furnace was washed with nitrogen atmosphere (purity 4.0) for 1 h. In the next step, the sample was heated at a rate of 10 °C·min$^{-1}$ to 1000 °C and kept at this temperature for 2 h. The cooling of the furnace was slow and took several hours after the process was stopped. The sample was held under a slight nitrogen overpressure throughout the process. The PPy-C yield from every bath of PPy-NT was between 39 and 47 %.

### 2.2. Preparation of samples for radar absorption measurement

PPy-NT and PPy-C powders were loaded into polydimethylsiloxane (PDMS) matrix in a ratio of 1–3 % w/w. The utilization of PDMS as matrices of herein studied samples has two advantages: i) it has a good ability to fill highly porous structure of conducting polymers (e.g., nanoplates, barrels, etc.) [19] and ii) it can be crosslinked by different approaches solving potential issues connected with a complex chemistry of conducting polymers.

Especially, PPy-NT was loaded into liquid Silgard 184 (2 components liquid PDMS; Dow Inc., USA) by a mechanical mixing in a beaker, poured into the 2 mm thick mold made of polytetrafluoroethylene (PTFE), degassed under low vacuum, and left 24 h for crosslinking.

Since PPy-C promoted an undesirable side reaction with the liquid Silgard 184 crosslinker, the procedure for loading it into PDMS was different. PPy-C was mechanically mixed in a two rolls mill (rolls 150 × 400 mm, friction 1:1.2, gap between rolls <1 mm, produced by Baťa company) with solid PDMS (G 1000, 0.17 mol.% vinyl groups, viscosity app. 1000 Pa s, high temperature vulcanizing silicone, Lučební závody Kolín). After mixing PPy-C into PDMS, a crosslinking agent (dicumyl peroxide – DCP, Sigma Aldrich) was added in the amount of 1 part per 100 parts of the mixture and it was also mixed on the two rolls mill. The hydraulic press was used to prepare a 150 × 150 mm sample in a mold with a thickness of 2 mm. The curing of the silicone mixture with PPy-C was carried out at 180 °C for 4 min with a compressive force of 250 kN. 80 g of the mixture was used to mold the samples. After molding, the samples were post-cured for 22 h at 170 °C in a hot air oven (to remove peroxide residues and to fix the network). Because of the high temperature of sample preparation, this method cannot be used for preparation of a PPy-NT/PDMS sample, whose stability of electrical conductivity under higher temperatures is lower.

The thickness of all the prepared samples was 2 mm and the area reached more than 200 cm$^2$. The thickness of the samples was in both procedures controlled by the geometry of the mold; moreover, prior to all calculations, the thickness of the sample was verified by micrometer. Later, sharp blade-made cutouts were used for radar absorption

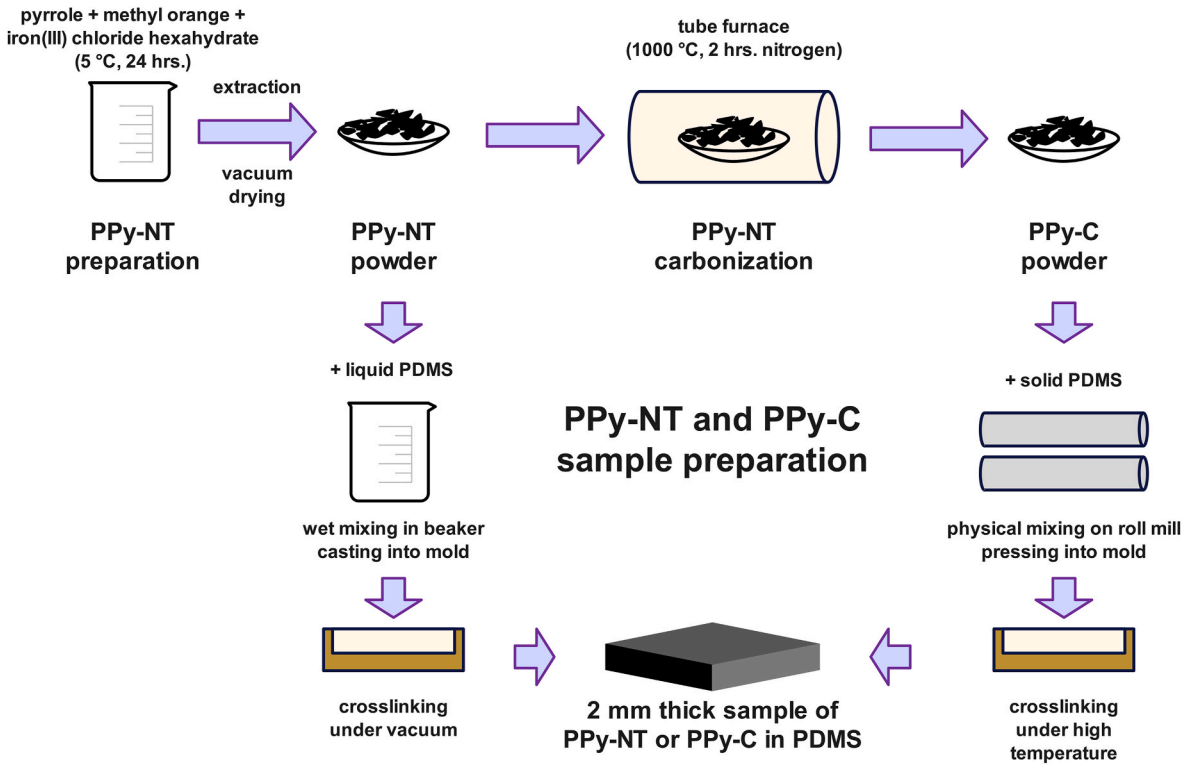


**Fig. 1.** Schematic illustration of the preparation method of PPy-NT and PPy-C samples used in the evaluation of radar absorption properties.

**Table 1**
Selected parameters of the waveguides used.

| Waveguide | Recommended frequency | Cutoff frequency lowest-order mode | Inner Dimensions for Waveguide Opening | |
|---|---|---|---|---|
| EIA denomination | GHz | GHz | *w* (mm) | *h* (mm) |
| WR284 | 2.60–3.95 | 2.078 | 72.1360 | 34.0360 |
| WR187 | 3.95–5.85 | 3.153 | 47.5488 | 22.1488 |
| WR137 | 5.85–8.20 | 4.301 | 34.8488 | 15.7988 |
| WR90 | 8.20–12.40 | 6.557 | 22.8600 | 10.1600 |
| WR62 | 12.40–18.00 | 9.488 | 15.7988 | 7.8994 |

measurement. The complete process of sample preparation for evaluation of radar absorption properties is depicted in Fig. 1.

### 2.3. Material characterization

Both the PPy-NT and PPy-C powders were characterized by Scanning Electron Microscopy (SEM), Transmission Electron Microscopy (TEM), Energy Dispersive X-ray (EDX) spectroscopy, Brunauer–Emmett–Teller (BET) specific surface measurement, and direct current (DC) electrical conductivity measurement.

SEM of the powdered samples was carried out on a Mira 3 LMH (Tescan Orsay) scanning electron microscope under 3 kV of accelerating voltage and EDX spectra were collected on the same system using a Quantax 200 with an XFlash 6|10 detector (Bruker) with a resolution of 127 eV and 15 kV of accelerating voltage.

BET was performed at 77 K using a static volumetric adsorption system (TriFlex analyzer, Micrometrics, Norcross, GA, USA). The adsorption isotherms were fitted to obtain the specific surface area and cumulative volume of the pores by the Barrett–Joyner–Halenda (BJH). The samples were incubated at 40 °C for 48 h under vacuum prior to adsorption measurements.

The DC electrical conductivity was measured on PPy-NT and PPy-C powders in a glass column under a defined pressure of 3 MPa. This method is described in detail by Kasparyan et al. [24].

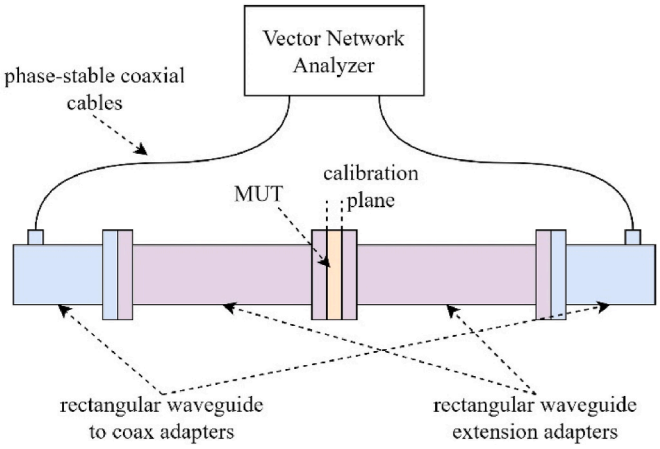


**Fig. 2.** Arrangement of the measuring workstation.

### 2.4. Apparatus for radar absorption measurement

The apparatus for radar absorption measurement consisted of a Rohde & Schwarz ZNB 20 vector network analyzer, two pieces of Rohde & Schwarz ZV-Z193 phase-stable coaxial cables, a set of rectangular waveguides for coaxial adapters (WR284, WR187, WR137, WR90 and WR62 – Table 1), a set of rectangular waveguide extension adapters to stabilize the EM field at the sample measurement location, and a set of waveguide holders to fix measured samples (Figs. 2 and 3a).

The measurement process was divided according to the frequency bands of each type of waveguide (WR284 - WR62). First, the configuration of the vector analyzer was performed. Specifically, this involved setting the frequency range (according to the waveguide), number of

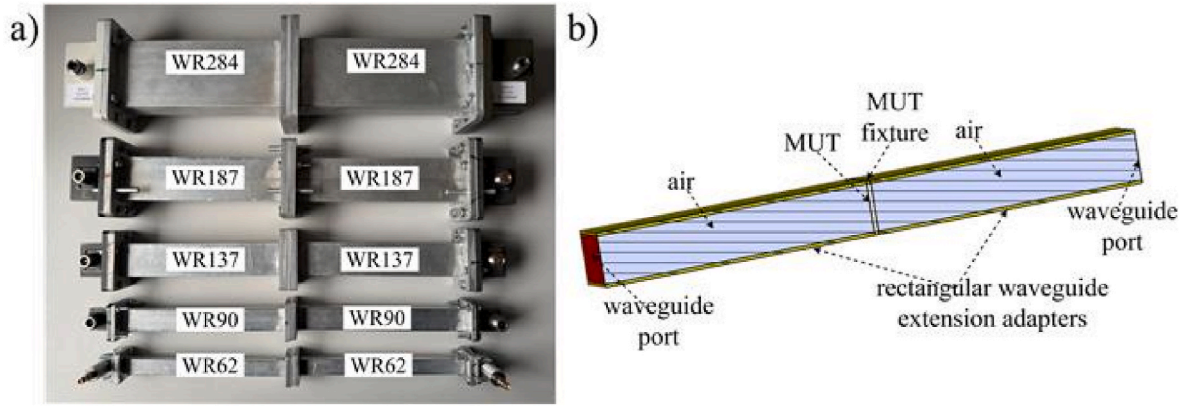


**Fig. 3.** Set of sample holders used for the waveguide method: a) photography and b) parametric simulation model in the cutaway view of WR 284 in CST Studio in the frequency range 2.6 and 18 GHz.

display points (5000), transmitted power (0 dBm), and the bandwidth of the frequency filter (1 kHz). The full two-port calibration was then carried out using the accurate and effective Transmission/Reflection Line (TRL) method. The method calibrates the sample plane to be measured, which fully suppresses the influence of the coaxial line, rectangular waveguide to coax adapters, and rectangular waveguide extension adapters on the measured sample. Different waveguide terminations are successively applied to the sample plane. Specifically, it is a "reflect" termination, which can just be a shorting plate; the "thru" termination, which includes simply connecting the two waveguide feeds directly together; and the "line," which corresponds to an extended "thru" with a phase shift of 20°–160°. This calibration method is limited to low accuracy when the sample length is close to the multiple of one-half wavelength in the material. After calibration, the waveguide holder with the material sample to be measured (Material Under Test, MUT) was inserted into the calibration plane. Subsequently, measurements of the scattering parameters of the MUT were made. Both the reflected power measurement $S_{11}$ and the transmitted signal measurement $S_{21}$ in a complex form were performed. Finally, an external program, METAS VNA Tools (Federal Institute of Metrology METAS, Switzerland), was used to convert the s-parameters to the dielectric properties using the appropriate conversion method.

Precise calibration and precise alignment of all parts of the waveguide significantly influence the quality of the measured results. There must be no air gaps within the waveguide and the sample must be accurately inserted into the holding frame.

Initial measurements of the s-parameters using a set of rectangular waveguides were performed on a well-defined material, a 3 mm thick polished polytetrafluoroethylene plate, whose dielectric properties are known in the literature [25,26]. The objective was to evaluate the design quality of the set and the mutual interdependency between the individual waveguides. The results of this measurement are also included in this work.

### 2.5. Calculations of dielectric and AC electrical properties

The calculation of the complex material permittivity and the loss tangent (tanδ) from s-parameters was performed using a METAS VNA Tools software, which was kindly provided by the Laboratory RF and Microwave, Federal Institute of Metrology METAS, Switzerland. Before the calculation, the port reference impedance of the s-parameters was changed to 1 Ω. The calculation method used was NIST Iterative [27] with set parameters Length 2 mm (thickness of the sample) and Cutoff Frequency (of the lowest-order mode) according to the selected waveguide; see Table 1.

The apparent AC electrical conductivity was calculated according to the procedure described in Moučka et al. [28]. Briefly, the apparent AC

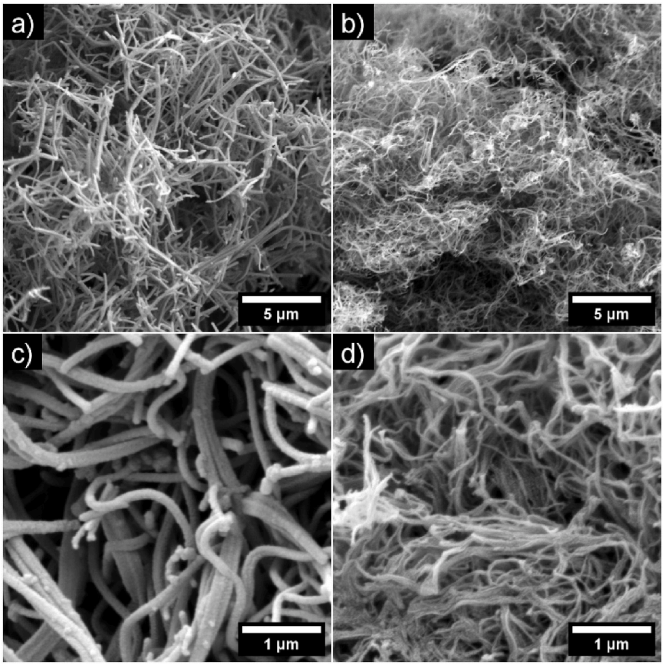


**Fig. 4.** Scanning electron microscopy analysis: images of PPy-NT (a,c) and PPy-C (b,d), respectively.

electrical conductivity is calculated as:

$$\sigma(\omega) = \omega\varepsilon_0\varepsilon'' \quad (1)$$

where $\omega$ is the angular velocity ($=2\pi f$), $\varepsilon_0$ denotes the permittivity of the vacuum, ε'' represents the loss part of the complex permittivity.

### 2.6. Simulation of s-parameters

Simulation of s-parameters based on calculated permittivity was performed in CST Studio Suite 2018 software, which is commonly used as a basic software tool for radar engineers designing antennas and radar systems. In this software, parametric models of all types of waveguides utilized (from WR62 to WR284) were created (Fig. 3b). The simulation model faithfully replicated the measurements performed. A conductive fixture was placed between two rectangular waveguide extension adapters, where a simulated material sample (MUT) was placed. The waveguides were excited by a homogeneous source of electromagnetic signal using waveguide ports, and the simulation was carried out using

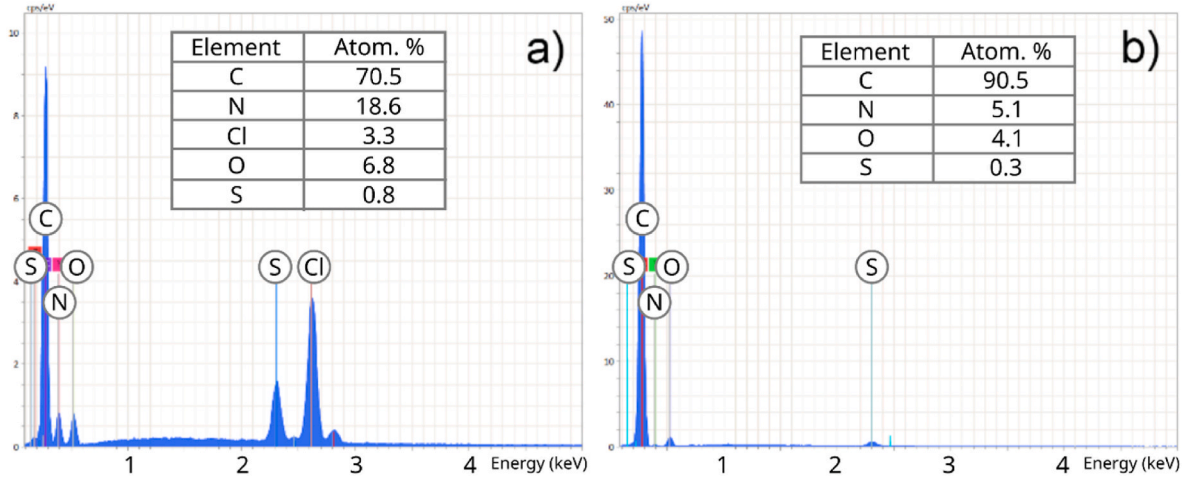


**Fig. 5.** Spectra of a) PPy-NT and b) PPy-C powders measured by EDX.

**Table 2**
Textural properties PPy-NT and C-PPy-NT measured by BET.

| Filler | $S_{BET}$ ($m^2g^{-1}$) | Total $V_{pore}$ $cm^3g^{-1}$ | $V_{mesopore}$ $cm^3g^{-1}$ | $V_{micropore}$ $cm^3g^{-1}$ | Pore diameter nm |
|---|---|---|---|---|---|
| PPy-NT [30] | 42.1 | 0.2253 | 0.2196 | 0.0057 | 21.36 |
| PPy-C | 1153.6 | 0.9949 | 0.8711 | 0.1238 | 3.45 |

only the dominant $TE_{10}$ mode. The use of this particular dominant mode corresponds to the frequency ranges used in accurate measurements.

The simulation model provides the creation and characterization of custom materials under test (MUTs). This characterization is done by inputting data on the frequency dependence of the relative permittivity of the material and the frequency dependence of the dissipation factor (loss tangent) of the material. The material sample fills the entire cross-section of the waveguide, and the parametric model allows us to vary its thickness.

## 3. Results and discussion

### 3.1. Physico-chemical, morphological, and textural properties of PPy-NT and PPy-C

PPy-NT and PPy-C underwent basic material characterizations to confirm their chemical structure and morphology (SEM and EDX) and to obtain their basic properties related to attenuating properties (specific surface and DC electrical conductivity).

Fig. 4 illustrates the ability of PPy-NT to retain nanotubular morphology after a 2-h treatment of PPy-NT under 1000 °C in nitrogen. However, diameter of nanotubes shrinks by high temperature and micropores are developed as also indicated by BET analysis. This is not a surprising result, as similar behavior was observed in our previous carbonization experiments, although at lower temperature (650 °C vs. 1000 °C) and significantly shorter duration (several seconds vs. 2 h) [29].

The progress of the carbonization process was further analyzed using EDX spectroscopy (Fig. 5). The results clearly indicate the conversion of the conducting polymer into an N-doped carbonaceous material. While this outcome was expected, it is important for the subsequent understanding of the radar attenuation mechanisms.

However, the nanotubular morphology of PPy-NT remains intact after intensive carbonization. The specific surface area tends to a substantial change, and the DC conductivity slightly decreases. The specific surface area measured by BET (see also Table 2) increased after carbonization from 42.1 $m^2\ g^{-1}$ for PPy-NT [30] to 1153.6 $m^2\ g^{-1}$ for PPy-C and the DC electrical conductivity decreased from 6.6 S $cm^{-1}$ for PPy-NT powder [24] to 3.1 S $cm^{-1}$ for PPy-C powder at 3 MPa. PPy-NT exhibits a mesoporous structure. During carbonization, microporosity also develops in PPy-C. However, the material predominantly retains its mesoporous character, which is further enhanced after carbonization. In theory, both trends should have a positive impact on the absorption properties of material at the expense of reflection. However, as will be shown and explained later, the results did not align with this expectation.

Finally, to complete the understanding of the carbonization process, it is important to mention the X-ray diffraction analysis carried out in previous experiments by Lapka et al. [30]. The PPy-NT material exhibits an amorphous structure, with the exception of weak diffraction peaks at 18° and 25°, which are attributed to residual methyl orange. During carbonization, methyl orange decomposes, while the amorphous nature of the material is retained.

### 3.2. Results of measurement of s-parameters

The magnitude and phase of the signals obtained using VNA, represented by the $S_{1,1}$ and $S_{2,1}$ parameters, across the full frequency range of 2.6–18 GHz, are shown in Fig. 6a,b and Fig. 6c,d, respectively, for the PTFE test samples.

The overall attenuation of PTFE in the range of 2.6–18 GHz is small, as expected (Fig. 6a and b). $S_{2,1}$ for the WR284 waveguide is near 0 dB and increases with frequency up to −1 dB for the WR62 waveguide, which corresponds to approx. 80 % of transmission (Fig. 6b), while $S_{1,1}$ starts at almost −18 GHz and quickly drops to −7 dB, which corresponds to approx. 20 % of reflection (with absorption being less than 1 %). There are almost negligible steps $\Delta S_{2,1}$ between each waveguide (Fig. 6b), which point to a well-selected and properly performed TRL calibration. The larger steps $\Delta S_{1,1}$ between the waveguides are given by larger proportional reflections in the waveguides with lower cross sections.

The signal curve is smooth for the WR284 and WR187 waveguides with lower frequencies and tends to develop periodic oscillations at higher frequencies, especially for the WR90 and WR62 waveguides. This is caused by interference of high frequencies with the geometry (especially thickness) of the PTFE plate. There are also two imperfections highlighted in the set of waveguides. The first denoted as $\Delta f_1$ is at the recommended 12.4 GHz frequency edge of the WR90 waveguide and is 200–300 MHz wide. The second one denoted as $\Delta f_2$ is at the recommended 18 GHz frequency edge of the WR62 waveguide and is about 500 MHz wide. Both imperfections, $\Delta f_1$ and $\Delta f_2$, are a result of the waveguide manufacturing process; the sensitivity of both high

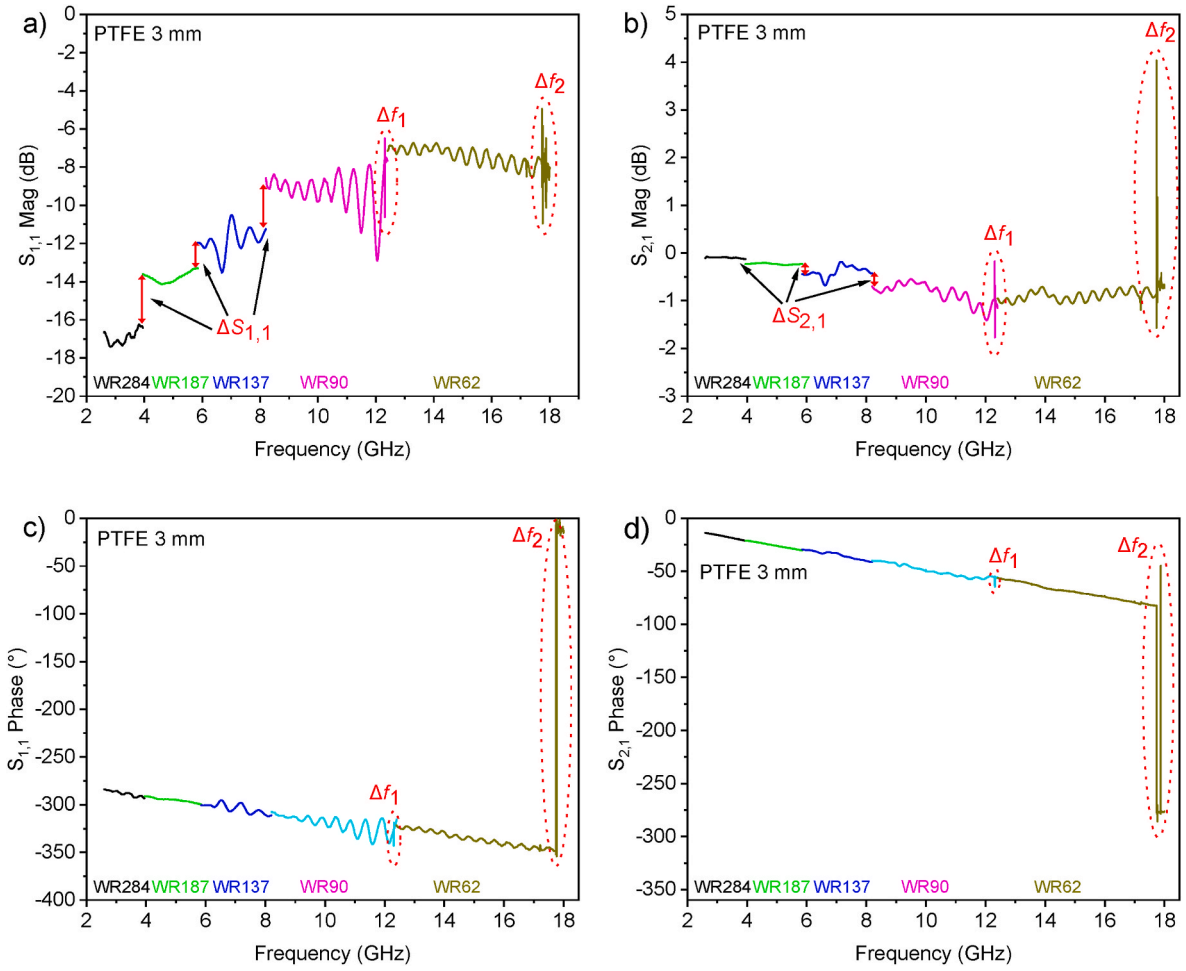


**Fig. 6.** Measurement of a, b) magnitude and c, d) phase of s-parameters $S_{1,1}$ and $S_{2,1}$ in the PTFE sample (3 mm thick) in the range of 2.6–18 GHz with highlighted imperfections.

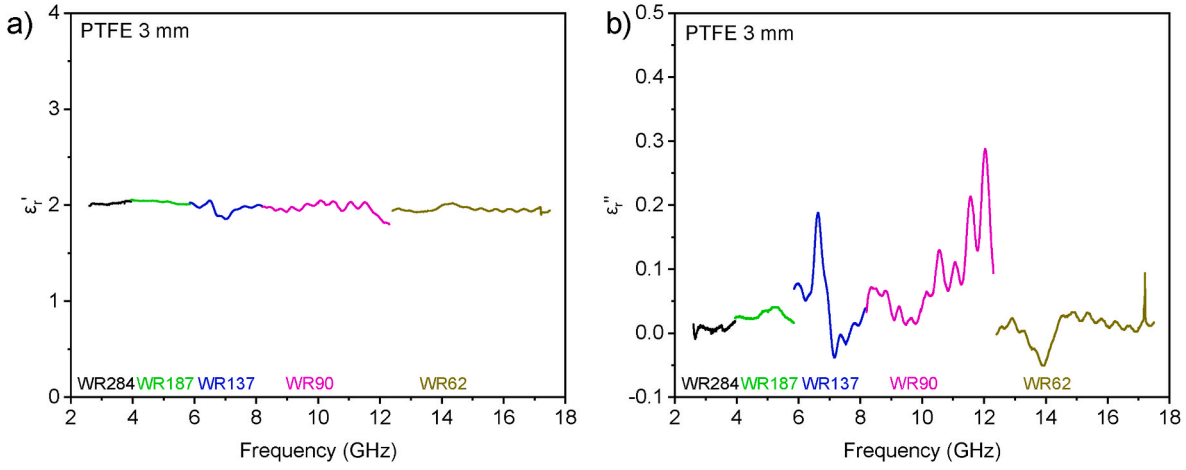


**Fig. 7.** Calculated dielectric parameters of PTFE in the range of 2.6–18 GHz: a) real part of complex electrical permittivity and b) imaginary part of complex electrical permittivity.

frequency measurement lines to geometrical imperfections of the waveguides is very high, and therefore the two signal imperfections cannot be calibrated off the line. Therefore, signals in the frequency range $\Delta f_1$ = 12.1–12.4 GHz and $\Delta f_2$ = 17.5–18 GHz will not be considered in all subsequent calculations.

The signal curve of the measured phase (Fig. 6c and d) is nicely continuous, again with two imperfections $\Delta f_1$ and $\Delta f_2$. The first one, $\Delta f_1$, is almost negligible whereas the second, $\Delta f_2$, is quite large. The $\Delta f_2$ is a combination of the poorer WR62 geometry (Fig. 6c and d) and the way in which VNA saves the phase output (specifically in Fig. 6c). After reaching a phase of −360°, the VNA changes the entire phase range starting from 0. This issue can be considered rather as a data problem

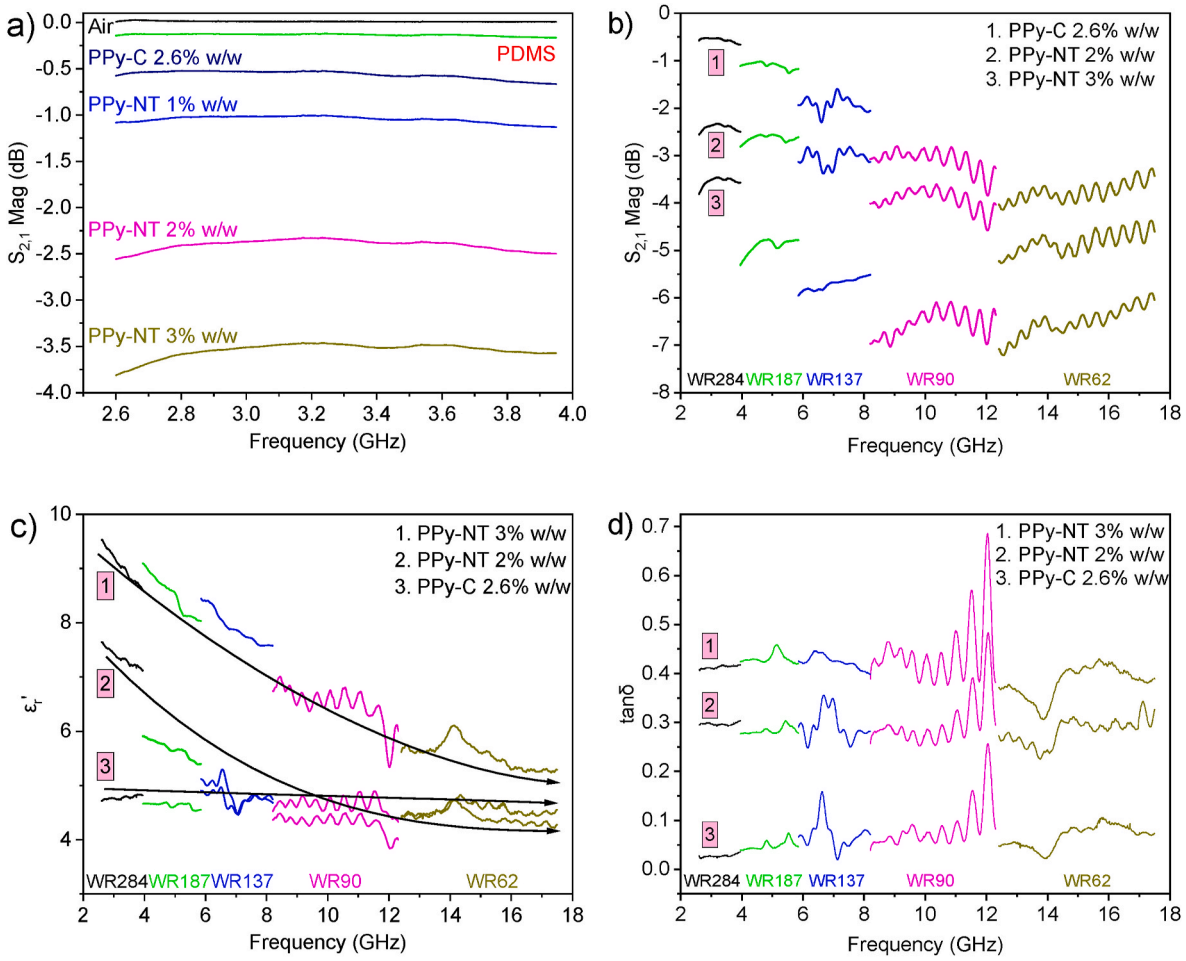


**Fig. 8.** Comparison of PPy-NT and PPy-C at various loads for different quantities: a) $S_{2,1}$ between 2.6 and 3.95 GHz of all samples, b) comparison of $S_{2,1}$ between 2.6 and 18 GHz for PPy-NT 2 % w/w, 3 % w/w and PPy-C loaded at 2.6 % w/w, c) comparison of the real part of complex permittivity, and d) comparison of the loss tangent.

(vital for precise calculation of permittivity using, e.g., the Nicholson-Ross-Weir method) and can be solved by data manipulation. However, since the NIST iterative permittivity calculation method was used, such manipulation was not necessary.

The calculations of permittivity using the NIST Iterative method in VNA Tools are straightforward. The complex permittivity of PTFE is shown in Fig. 7a and b. The real part of permittivity, denoted as ε′, is frequency independent, almost constant around 2.0, which is in good agreement with the literature [25,26]. The imaginary part of the permittivity, denoted as ε'', is generally very low, between 0 and 0.3, indicating a low loss material.

Once all pitfalls of s-parameter measurement on PTFE in the broad range of 2.6–18 GHz were identified, measurements were performed on the prepared samples, PPy-NT and PPy-C, whose behavior was previously unknown. Fig. 8a shows a detailed comparison of the $S_{2,1}$ parameter in WR284. The measurement was carried out in an air gap of the size equal to the sample thickness (2 mm), in a pure PDMS plate equal to the sample thickness, in samples with 1, 2, and 3 % w/w of PPy-NT in PDMS and finally in the sample with 2.6 % w/w of PPy-C in PDMS. The results indicate that both the air gap and PDMS have negligible influence on the magnitude of $S_{2,1}$. $S_{2,1}$ of PPy-NT 3 % w/w in WR284 is around −3.5 dB corresponding to 55.8 % of attenuation (27.3 % reflection and 28.5 % absorption). The best attenuation properties were achieved in the frequency range of WR62 equal to 77.7 % (49.7 % reflection and 28 % absorption). The absorption properties of PPy-NT, important for RAMs, are clearly independent of frequency, whereas undesirable reflection increases with frequency. Generally, the absorption properties of PPy-NT are rather mediocre for practical applications, but considering the amount (3 % w/w), the thickness (2 mm), and the purely organic nature of the material, it is not insignificant. The high flexibility of the sample, which is unusual for common materials utilized in RAMs, must also be highlighted. Finally, as expected, the ability of PPy-NT to attenuate the electromagnetic signal decreases with load (Fig. 8b).

The $S_{2,1}$ parameter of PPy-C 2.6 % w/w is low, even lower than that of PPy-NT 1 % w/w (Fig. 8a). The attenuation ability of PPy-C is better at higher frequencies of WR62 (58.1 % attenuation; 50 % reflection and 8.1 % absorption), which means that the carbonization of PPy-NT leads to better reflection at the cost of absorption (Fig. 8b). It seems that N-doped carbon nanotubes cannot reach a high level of absorption properties, which is probably given by their high conductivity and low dipole content, which is decreased during the conversion of PPy-NT onto PPy-C.

This idea can be supported by the calculated dielectric properties (Fig. 8c). While the real part of the permittivity ε′ of PPy-NT is frequency dependent and a large relaxation of the dipoles and charge carriers can be observed in the broad frequency range, PPy-C devoid of charge carriers and several polar molecules has a low and almost constant real part of the permittivity ε' (Fig. 8c). The result of the PPy-C permittivity calculation also indicates the structural uniformity and low dispersion of this type of carbon nanotubes.

To fully illustrate the shielding properties of all samples, their loss tangents are depicted in Fig. 8d. The PPy-C sample is a typical low loss material, while the PPy-NT 3 % w/w sample with tanδ higher than 0.4

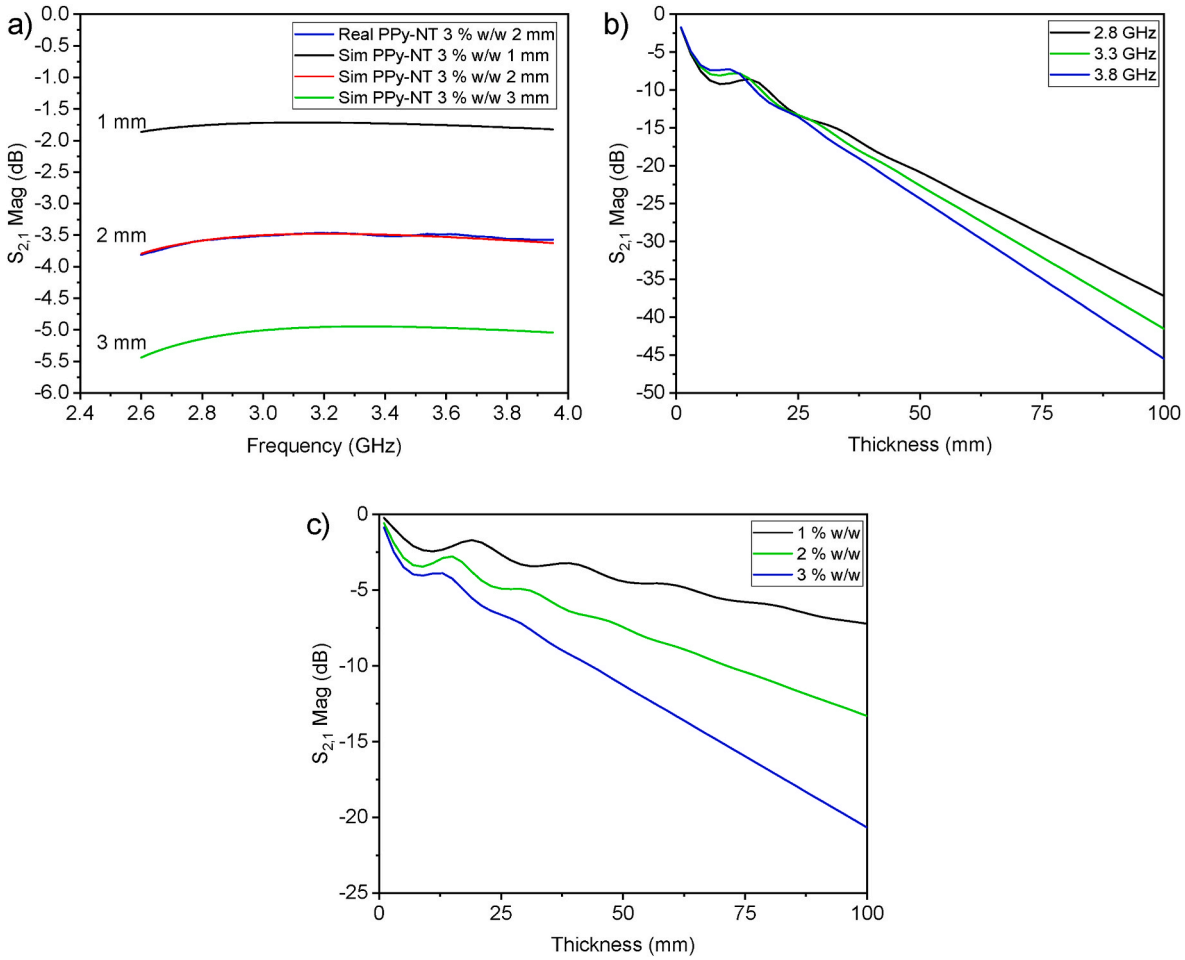


**Fig. 9.** Simulation of s-parameters for various thicknesses: a) comparison of PPy-NT 3 % w/w 2 mm thick vs. simulated PPy-NT 3 % w/w 1 and 2 mm thick in WR284, b) simulations of the attenuation properties of PPy-NT 3 % w/w between 0 and 100 mm at various frequencies, c) simulations of the attenuation properties of PPy-NT 1, 2 and 3 % w/w between 0 and 100 mm at the frequency of 3.3 GHz.

falls into lossy materials.

Mathematical simulation of s-parameter measurement is not only a vital tool for radar engineers, but it can be very useful for material chemists. Here, simulations were carried out with two objectives in mind.

The first objective was to obtain feedback on our measurements using two independent algorithms. While VNA Tools was intended solely for calculation of the dielectric parameters of the presented samples, the verification of s-parameter measurements was made using CST Studio on the models of all used waveguides. This verification is shown in Fig. 9a. Using dispersive parameters (i.e. frequency-dependent dielectric properties), measured on real samples in a model of waveguides programed in CST Studio, resulted in frequency-dependent s-parameter curves. Fig. 9a shows simulation of frequency-dependent s-parameter curves of PPy-NT 3 % w/w for various thicknesses (1, 2 and 3 mm). All of them were simulated using the original permittivity calculated on a 2 mm thick sample of PPy-NT 3 % w/w in PDMS. Both curves for the 2 mm thick real and simulated samples fit perfectly.

The second objective was to extend the current results measured in samples of 1, 2 and 3 mm thick by simulation on theoretical samples of the same composition but with various thicknesses (Fig. 9b and c). The advantage of simulation in this case is obvious. The optimal thickness of the sample to achieve 99.99 % attenuation can be quickly estimated for various frequencies (Fig. 9b) or different compositions (Fig. 9c). For example, 99.99 % attenuation (63 % absorption and 37 % reflection) is achieved on the PPy-NT 3 % w/w sample at 3.3 GHz when the sample is 95 mm thick (Fig. 9b). The same thickness estimation can be made for various compositions (Fig. 9c). Moreover, in the future it will also be possible to assess the load (% w/w) necessary for a particular attenuation, although this simulation needs more reference data than presented in Fig. 9c, for example, the mechanical stability of highly loaded

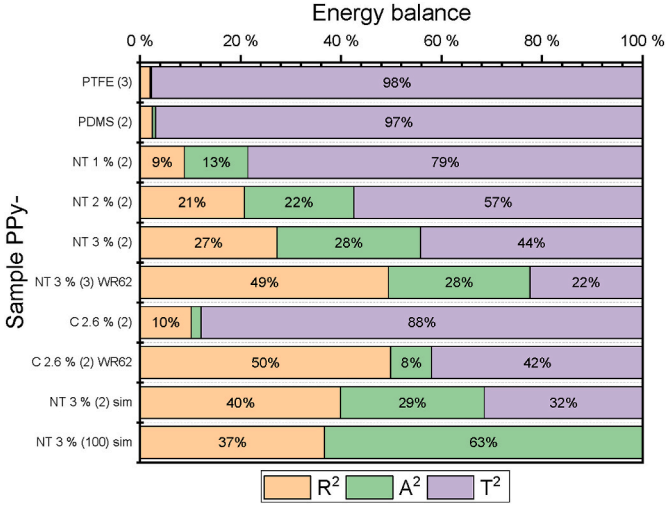


**Fig. 10.** Results of the RAT analysis of the PPy-NT and PPy-C samples on WR284 (with two exceptions WR62 mentioned in the legend of the figure).

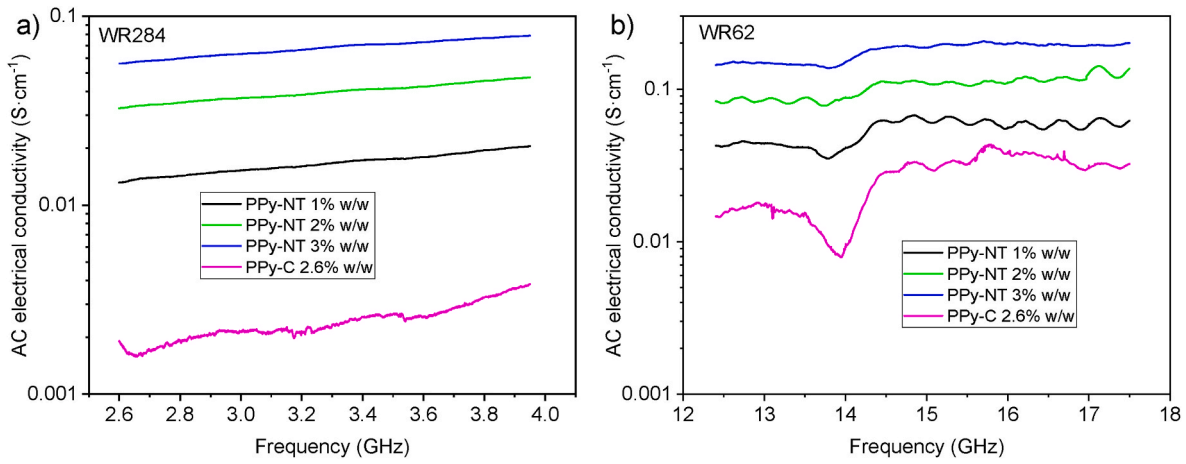


**Fig. 11.** Apparent AC conductivity of PPy-NT and PPy-C at the beginning and end of the frequency range a) WR284 2.6–3.95 GHz, b) WR62 12.4–17.5 GHz.

samples. The results of these simulations have very practical consequences. In materials chemistry, it is very common that newly prepared substances are available in small quantities (either the large-scale preparation is difficult at the beginning or is very expensive). Simulation of s-parameters using dispersive data measured on highly diluted or small samples can be vital for predetermination of broadband radar attenuation properties.

The energy balance of all important real and simulated samples is summarized in the RAT analysis in Fig. 10. From Fig. 10, it is clear that PPy-NT is favorable for its absorption properties, which increase with the thickness of the sample. The highest absorption properties (63 %) are again found in the case of thick (>95 mm) simulated samples. However, considering practical application, such a thickness is not suitable for functional composites used in the form of, e.g., paintings, but because PPy-NT can be easily compatibilized with conventional polymers, its convenient utilization as a filler of structural composites is offered. The energy balance also reveals that conversion of PPy-NT onto PPy-C leads to a loss of absorption properties and the development of large reflections at high frequencies.

Finally, knowledge of the sample permittivity serves to calculate the apparent AC conductivity. Fig. 11 shows the apparent AC conductivity of all samples in WR284 and WR62. The AC conductivity of PPy-NT between 2.6 and 17.5 GHz is only changing very slightly. On the other hand, a substantial increase in the AC conductivity for PPy-C can be explained in terms of its high reflection coefficient on WR62.

## 4. Conclusions

The development of novel nanostructured electrically conductive materials brings new opportunities for the construction of UAVs or UGVs protected against radar detection or electromagnetic countermeasures. Herein, polypyrrole-based materials, i.e. PPy-NT and PPy-C, have been demonstrated as RAMs. The targeted property was the absorption of the radar signal that reached around 28 % in the frequency band of 2.6–18 GHz for PPy-NT 3 % w/w; the total attenuation of the same material reached 78 % in the frequency range of 12.4–18 GHz. The practical implementation of such a material takes advantage of its ability to be compatible with conventional polymers in structural composites. Furthermore, simulations performed on the model of the sample in the waveguide predicted the behavior of the material beyond the physical boundaries of the real sample. Under these conditions, a theoretical 95 mm-thick PPy-NT sample (3 % w/w) would attenuate 99.99 % of the incoming electromagnetic radiation, with approximately 63 % absorbed and 37 % reflected.

Although both tested materials deserve more future development to improve the absorption component of radar attenuation (e.g., the addition of magnetic nanoparticles is a common approach), the results of this work have practical implications.

In materials chemistry, it is very common for newly prepared substances to be available in small quantities (large-scale preparation is either difficult at the beginning or very expensive). Simulation of s parameters using dispersive data measured on highly diluted or small samples can be vital for the predetermination of broadband radar attenuation properties. From this point of view, the authors believe that this work will find its audience.

## CRediT authorship contribution statement

**Tomáš Zálabský:** Software, Project administration, Methodology, Investigation, Funding acquisition, Data curation, Conceptualization. **Drahomír Čadek:** Methodology, Investigation. **Fatima Hassouna:** Methodology, Investigation. **Jiří Tuček:** Validation, Methodology. **Tomáš Lapka:** Investigation, Writing – review & editing. **Dušan Kopecký:** Writing – original draft, Methodology, Investigation, Data curation, Conceptualization.

## Data statement

The data are available in the Zenodo repository (https://doi.org/10.5281/zenodo.15357037).

## Declaration of competing interest

The authors declare that they have no known competing financial interests or personal relationships that could have appeared to influence the work reported in this paper.

## Acknowledgment

The work was supported from ERDF "Multi-sector and Interdisciplinary Cooperation in Research and Development of Communication, Information and Detection Technologies for Control and Signalling Systems (CIDET)" (No. CZ.02.01.01/00/23_021/0008402).

We would like to thank Dr. Jan Prokeš for DC electrical conductivity measurement and assoc. prof. Miloslav Lhotka for BET analysis.

## Data availability

Data are available in the Zenodo repository (https://doi.org/10.5281/zenodo.15357037).

## References


[1] W. Khawaja, V. Semkin, N.I. Ratyal, Q. Yaqoob, J. Gul, I. Guvenc, Threats from and countermeasures for unmanned aerial and underwater vehicles, Sensors 22 (10) (2022) 3896, https://doi.org/10.3390/s22103896.

[2] Y. Yao, F. Shu, X. Cheng, H. Liu, P. Miao, L. Wu, Automotive radar optimization design in a spectrally crowded V2I communication environment, IEEE Trans. Intell. Transport. Syst. 24 (8) (2023) 8253–8263, https://doi.org/10.1109/TITS.2023.3264507.

[3] A. Kolanowska, D. Janas, A.P. Herman, R.G. Jędrysiak, T. Giżewski, S. Boncel, From blackness to invisibility – carbon nanotubes role in the attenuation of and shielding from radio waves for stealth technology, Carbon 126 (2018) 31–52, https://doi.org/10.1016/j.carbon.2017.09.078.

[4] N. Devi, S.S. Ray, Electromagnetic interference cognizance and potential of advanced polymer composites toward electromagnetic interference shielding: a review, Polym. Eng. Sci. 25876 (2022), https://doi.org/10.1002/pen.25876 pen.

[5] S. Kim, S. Lee, Y. Zhang, S. Park, J. Gu, Carbon-based radar absorbing materials toward stealth technologies, Adv. Sci. 10 (32) (2023) 2303104, https://doi.org/10.1002/advs.202303104.

[6] M. Popescu, V. Bîndar, R. Craciunescu, O. Fratu, Estimate of minimum attenuation level for a TEMPEST shielded enclosure, in: 2016 International Conference on Communications (COMM), 2016, pp. 513–518, https://doi.org/10.1109/ICComm.2016.7528278.

[7] Y. Zhang, J. Gu, A perspective for developing polymer-based electromagnetic interference shielding composites, Nano-Micro Lett. 14 (1) (2022) 89, https://doi.org/10.1007/s40820-022-00843-3.

[8] B. Xie, Q. Li, Y. Zhang, C. Yuan, High-frequency electromagnetic behavior, impedance modeling, and enhancement of low-permeability powder cores, IEEE Trans. Power Electron. 40 (2) (2025) 3336–3356, https://doi.org/10.1109/TPEL.2024.3488117.

[9] G. Zhou, J. Huang, H. Li, Y. Li, G. Jia, N. Song, J. Xiao, Multispectral camouflage and radiative cooling using dynamically tunable metasurface, Opt. Express 32 (7) (2024) 12926, https://doi.org/10.1364/OE.517889.

[10] K. Zou, S. Yi, X. Li, J. Li, Y. Xu, Z.-M. Li, D.-X. Yan, H. Wang, Efficient electromagnetic interference shielding of flexible Ag microfiber sponge/polydimethylsiloxane composite constructed by blow spinning, Compos. Sci. Technol. 220 (2022) 109281, https://doi.org/10.1016/j.compscitech.2022.109281.

[11] V. Shukla, Review of electromagnetic interference shielding materials fabricated by iron ingredients, Nanoscale Adv. 1 (5) (2019) 1640–1671, https://doi.org/10.1039/C9NA00108E.

[12] Y. Zhao, S. Xing, Q. Jin, N. Yang, Y. He, J. Zhang, Excellent angular and electrical performance damage tolerance of wave-absorbing laminate via gradient A-T-A design, Compos. Commun. 46 (2024) 101838, https://doi.org/10.1016/j.coco.2024.101838.

[13] J.-T. Liu, Y.-C. Zheng, X. Hou, X.-R. Feng, K. Jiang, M. Wang, Structured carbon for electromagnetic shielding and microwave absorption from carbonization of waste polymer: a review, Chem. Eng. J. 496 (2024) 154013, https://doi.org/10.1016/j.cej.2024.154013.

[14] B. Dai, Overview of MXene and conducting polymer matrix composites for electromagnetic wave absorption, Adv. Compos. Hybrid Mater. 51 (2022).

[15] X. Liu, B. Zheng, Y. Hua, S. Lu, Z. Nong, J. Wang, Y. Song, Ultralight MXene/rGO aerogel frames with component and structure controlled electromagnetic wave absorption by direct ink writing, Carbon 230 (2024) 119650, https://doi.org/10.1016/j.carbon.2024.119650.

[16] K.S. Sista, S. Dwarapudi, D. Kumar, G.R. Sinha, A.P. Moon, Carbonyl iron powders as absorption material for microwave interference shielding: a review, J. Alloys Compd. 853 (2021) 157251, https://doi.org/10.1016/j.jallcom.2020.157251.

[17] N. Maruthi, M. Faisal, N. Raghavendra, Conducting polymer based composites as efficient EMI shielding materials: a comprehensive review and future prospects, Synth. Met. 272 (2021) 116664, https://doi.org/10.1016/j.synthmet.2020.116664.

[18] Y. Sood, H. Mudila, P. Chamoli, P. Saini, A. Kumar, Exploring the efficacy and future potential of polypyrrole/metal oxide nanocomposites for electromagnetic interference shielding: a review, Mater. Horiz. 11 (18) (2024) 4256–4274, https://doi.org/10.1039/D4MH00594E.

[19] R. Moučka, M. Sedlačík, J. Prokeš, H. Kasparyan, S. Valtera, D. Kopecký, Electromagnetic interference shielding of polypyrrole nanostructures, Synth. Met. 269 (2020) 116573, https://doi.org/10.1016/j.synthmet.2020.116573.

[20] L. Lu, J. Le, L. Zhang, S. Shen, X. Ren, Polarization independent tunable near-perfect absorber based on graphene-BaO arrays and Ag-dielectric bragg reflector composite structure, Diam. Relat. Mater. 152 (2025) 111958, https://doi.org/10.1016/j.diamond.2025.111958.

[21] D. Kopecký, M. Varga, J. Prokeš, M. Vrňata, M. Trchová, J. Kopecká, M. Václavík, Optimization routes for high electrical conductivity of polypyrrole nanotubes prepared in presence of methyl orange, Synth. Met. 230 (2017) 89–96, https://doi.org/10.1016/j.synthmet.2017.06.004.

[22] T. Lapka, J. Vilčáková, D. Kopecký, J. Prokeš, M. Dendisová, R. Moučka, M. Sedlačík, F. Flexible Hassouna, Ultrathin and light films from one-dimensional nanostructures of polypyrrole and cellulose nanofibers for high performance electromagnetic interference shielding, Carbohydr. Polym. 309 (2023) 120662, https://doi.org/10.1016/j.carbpol.2023.120662.

[23] J. Stejskal, M. Trchová, Conducting polypyrrole nanotubes: a review, Chem. Pap. 72 (7) (2018) 1563–1595, https://doi.org/10.1007/s11696-018-0394-x.

[24] H. Kasparyan, F. Hassouna, J. Prokeš, I. Křivka, M. Lhotka, M. Trchová, P. Sialini, D. Kopecký, Electromechanical properties of melamine foams covered by polypyrrole nanotubes and carbonaceous fillers, Sensor Actuator Phys. (2023) 114160, https://doi.org/10.1016/j.sna.2023.114160.

[25] J. Krupka, Measurements of the complex permittivity of low loss polymers at frequency range from 5 GHz to 50 GHz, IEEE Microw. Wireless Compon. Lett. 26 (6) (2016) 464–466, https://doi.org/10.1109/LMWC.2016.2562640.

[26] U.C. Hasar, O. Simsek, An accurate complex permittivity method for thin dielectric materials, PIER 91 (2009) 123–138, https://doi.org/10.2528/PIER09011702.

[27] J. Baker-Jarvis, E.J. Vanzura, W.A. Kissick, Improved technique for determining complex permittivity with the transmission/reflection method, IEEE Trans. Microw. Theor. Tech. 38 (8) (1990) 1096–1103, https://doi.org/10.1109/22.57336.

[28] R. Moučka, M. Sedlačík, H. Kasparyan, J. Prokeš, M. Trchová, F. Hassouna, D. Kopecký, One-dimensional nanostructures of polypyrrole for shielding of electromagnetic interference in the microwave region, Int. J. Mol. Sci. 21 (22) (2020) 8814, https://doi.org/10.3390/ijms21228814.

[29] J. Kopecká, M. Mrlík, R. Olejník, D. Kopecký, M. Vrňata, J. Prokeš, P. Bober, Z. Morávková, M. Trchová, J. Stejskal, Polypyrrole nanotubes and their carbonized analogs: synthesis, characterization, gas sensing properties, Sensors 16 (11) (2016) 1917, https://doi.org/10.3390/s16111917.

[30] T. Lapka, D. Kopecký, P. Mazúr, J. Prokeš, P. Ulbrich, M. Dendisová, M. Sedlačík, F. Hassouna, Elaboration and properties of nanofibrillated cellulose composites with polypyrrole nanotubes or their carbonized analogs, Synth. Met. 278 (2021) 116806, https://doi.org/10.1016/j.synthmet.2021.116806.